



# Influence of the electrochemical processing parameters on the photocurrent–voltage conversion characteristics of copper bismuth selenide photoactive films

M. S. Eraky<sup>1</sup>, Moustafa M. S. Sanad<sup>1,a</sup>, E. M. El-Sayed<sup>1</sup>, Atef Y. Shenouda<sup>1</sup>, El-Sayed El-Shereafy<sup>2</sup>

<sup>1</sup> Chemical and Electrochemical Processing Department, Central Metallurgical Research and Development Institute, P. O. Box 87, Helwan, Cairo 11421, Egypt

<sup>2</sup> Chemistry Department, Faculty of Science, Menoufia University, Shebin El-Kom, Egypt

Received: 24 October 2021 / Accepted: 5 July 2022

© The Author(s) 2022

**Abstract** Thin-film deposition using electrodeposition techniques is highly preferable because of its capability to deposit multi-component alloys at low temperatures. In this regard, copper bismuth selenide (CBSe) films were electrodeposited in two various ways, simultaneous and successive electrodeposition processes. The structural and morphological characterizations of the obtained films were performed using X-ray diffraction (XRD), scanning electron microscope (SEM), energy-dispersive X-ray analysis (EDX), and X-ray Photoelectron Spectrometer (XPS). The CBSe alloy films formed by successive electrodeposition revealed better crystallinity and more regular morphology in comparison with simultaneous electrodeposited CBSe films. The prepared CBSe film by successive electrodeposition exhibited high light absorptivity and low band gap energy value ( $E_g = 1.65$  eV) resulting in a higher photoelectrical response. The crystallization of the ternary CBSe film electrodeposited via successive routine obeyed the instantaneous nucleation mechanism, while the CBSe film obtained by simultaneous electrodeposition agreed with the progressive nucleation mechanism. Successive electrodeposition of ternary CBSe alloy film achieved greater values of photocurrent–voltage conversion efficiency ( $\eta = 1.26\%$ ) in photoelectrochemical systems.

## 1 Introduction

Metal-based chalcogenides have been emerged as one of the most important classes of semiconducting materials due to their multidisciplinary uses in photovoltaic (PV), optoelectronic and thermoelectric applications [1–3]. Chalcogenide is an inorganic compound that contains one or more chalcogen elements such as O, S, Se, or Te of the group 16 in the Periodic Table [4, 5]. Chalcogenides are usually alloyed with other elements of metallic, non-metallic, or even another semiconductor to form a matrix, which could be applied in the aforementioned applications, especially in solar cells [6, 7]. Different elements were employed for the preparation of chalcogenide materials like Cd, Ga, In, Zn, As, Cu, and Ag [8–10]. Among all these elements, copper is still recognized as a cost-effective, environmentally benign, and highly abundant metal. Considering this fact, huge considerable efforts have been devoted to preparing copper-based chalcogenides of the groups (I–V–VI) acting as efficient light absorbers for upgrading thin-film PV applications [11, 12]. Particularly, Cu–Bi–Se (CBSe) ternary system has recently attracted much attention, because the usage of Cu–Bi–Se (CBSe) thin-film demonstrates a high absorption coefficient  $> 10^5$  cm<sup>-1</sup> and a wide bandgap range of 1.2–1.5 eV as well as good photoactivity for solar light absorption [11, 13]. Consequentially, these distinguishable features and characteristics give the CBSe material with its various systems the opportunity in different applications mainly as light harvesting materials in PV thin film solar cells and photocatalytic applications as reported in different previous studies [11, 14]. In addition, CBSe materials possess high photosensitivity that generates a considerable photocurrent revealing its ability for optoelectronic devices [15].

Unlike various methods, e.g., thermal evaporation, chemical vapor deposition (CVD), physical vapor deposition (PVD), and sputtering which are employed for film deposition, the electrodeposition process is considered the most applicable technique to form thin-film material on large conductive surfaces [16]. It is able to produce a dense, uniform, and adherent coating either from metal or alloys on regular or irregular shaped substrates by applying an electric current [17]. Besides, electrodeposition is clean, accurate, short-time, and sometimes energy-saving technique, because it is usually working at low temperatures below 100 °C or even at room temperature [18, 19]. However, the electrodeposition of ternary metallic alloys is still facing some difficulties that could reduce its competitiveness with the other film deposition methods. Among these drawbacks, the high sensitivity for any contamination or additive that existed in the medium affects the deposition process and the formed film. Also, the low conductivity of some semiconducting elements makes their deposition potential shift toward the positive value for the noble elements that increase the possibility of co-deposition of undesired elements with the target alloy [17]. Therefore, various parameters affecting the electrodeposition process such as current density, deposition potential, scan rate, concentration, temperature, additives, nature

<sup>a</sup> e-mail: [mustafa\\_sanad2002@yahoo.com](mailto:mustafa_sanad2002@yahoo.com) (corresponding author)

of the electrolyte, nature of substrate, deposition time, and agitation should be chosen carefully and accurately to obtain the target film with the proper planned properties [17, 19].

The electrodeposition of thin-film alloys can be carried out in different ways including successive and simultaneous paths [20]. Concerning the literature survey and in our humble belief, only one published article discussed the preparation of CBSe thin film on SnO<sub>2</sub>-coated glass substrate via potentiostatic electrodeposition simultaneously from a solution mixture of CuCl<sub>2</sub>, Bi(NO<sub>3</sub>)<sub>3</sub>, and H<sub>2</sub>SeO<sub>3</sub> followed by post-annealing treatment [14]. The simultaneous electrodeposition of the ternary alloy system is not effective enough, because the three ions compete with each other in the deposition process, which does not give the metallic component sufficient time to be electrodeposited effectively and progressively than the other components. As a result, the metallic component of the formed ternary alloy might be larger than the semiconductor and non-metallic content (i.e., non-stoichiometric ternary alloy). In this regard, the present work aims to study the electrochemical deposition of CBSe films on the platinum substrate via both successive (indirect) and simultaneous (direct) ways from an aqueous solution of Cu(NO<sub>3</sub>)<sub>2</sub>, Bi(NO<sub>3</sub>)<sub>3</sub>, and SeO<sub>2</sub>. The novel suggested successive way starts by depositing a film of two metallic components as binary alloy from a solution containing the two ionic species. Subsequently, the third element is deposited from its containing solution. This allows forming of the binary alloy easily and effectively in the first stage, which serves as a substrate for the second layer. Thereby, the ternary alloy can be significantly obtained after heat treatment. The structural and morphological properties of CBSe thin films on a platinum substrate prepared by successive and simultaneous electrodeposition were comparatively investigated. The deposition mechanism was predicted by applying Scharifker and Hills Model. The film thickness and current efficiency of CBSe deposited films were mathematically calculated from the chrono-potentiometric studies at various current densities. Finally, the as-deposited photoactive CBSe electrodes were characterized for their photovoltaic performance in photoelectrochemical solar cells.

## 2 Experimental

### 2.1 Materials

The following materials were employed throughout this work as follows: copper nitrate trihydrate Cu(NO<sub>3</sub>)<sub>2</sub>·3H<sub>2</sub>O (≥ 99%, LOBA Chemie), selenium dioxide SeO<sub>2</sub> (99%, LOBACHemie), bismuth nitrate pentahydrate Bi(NO<sub>3</sub>)<sub>3</sub>·5H<sub>2</sub>O (≥ 99.5%, CARLO ERBA), ammonium nitrate NH<sub>4</sub>NO<sub>3</sub> (≥ 99%, LABKEM), nitric acid HNO<sub>3</sub> (65%, MERK), ethanol absolute C<sub>2</sub>H<sub>5</sub>OH (99%, ChemLab), acetone (CH<sub>3</sub>)<sub>2</sub>CO (≥ 99%, ChemLab), ammonium hydroxide NH<sub>4</sub>OH (30%, LabChem), indium tin oxide (ITO)-coated glass substrate, total area 25 × 25 mm<sup>2</sup>, ITO thickness ~ 185 nm, sheet resistance ~ 6–8 Ohm/sq, Transmittance > 84% (BIOTAIN).

### 2.2 Electrodeposition processes

The electrodeposition process was performed in a 150 ml three-electrode glass cell in which a platinum mesh of area 4 cm<sup>2</sup> was implemented as the counter electrode. The working electrode is a platinum sheet and ITO-coated glass of active area 2 cm<sup>2</sup> for deposition, while the silver/silver chloride was used as a reference electrode [ $E = 0.197$  mV vs. NHE]. The electrochemical deposition process was carried out and controlled using potentiostat/galvanostat Volatalab Master PGP 201. Before deposition, Pt and ITO-coated glass substrates were ultrasonically cleaned using different solvents in the order of acetone, ammonia, ethyl alcohol, and then rinsed with deionized water. Linear sweep voltammetry (LSV) studies were carried out for unitary, binary, and ternary components of the target material. Sweeping potentials for Cu-Se, and CBSe solutions were ranged from – 800 to 200 mV and – 1000 to 300 mV, respectively. The stirring rates were varied from 0 to 800 rpm through an automated digital hotplate with well-defined stirring rates. Three bath temperatures were studied 25, 50, and 75 °C using a thermostat. The applied potential scan rates were varied from 1 to 10 mV/s. After that, potentiostatic and galvanostatic electrodeposition measurements were performed at different potential and current density values concluded from the LSV curves. The obtained potentiostatic data were used to study the nucleation mechanisms during the first 5 s of the deposition process using Scharifker and Hills models. Galvanostatic results were used to calculate the current efficiency by weighing the Pt substrate before and after deposition to calculate the weight and thickness of the deposited film considering the density related to the obtained phase. The optimal conditions were applied for the deposition of the films on the ITO glass to perform the optical and photoelectrochemical characterizations. The electrodeposition of CBSe films was performed in two different ways successive and simultaneous as follows

*Successive electrodeposition* in which ternary CBSe film was prepared through two successive steps. At the first step, binary Cu-Se film was galvanostatically deposited on the platinum substrate, from 80 ml solution (pH ~ 3) consisting of 50 mM Cu(NO<sub>3</sub>)<sub>2</sub>·3H<sub>2</sub>O + 100 mM SeO<sub>2</sub>. Few drops of 0.5 M NH<sub>4</sub>NO<sub>3</sub> were added as a supporting agent. Subsequently, the second galvanostatic electrodeposition of Bi metal on the deposited Cu-Se film was carried out from 80 ml solution of 50 mM Bi(NO<sub>3</sub>)<sub>3</sub>·5H<sub>2</sub>O. Few drops of conc. nitric acid were added to the bismuth nitrate solution to ensure the solubility of the salt and the solution pH was kept at 2.

*Simultaneous electrodeposition* in which ternary CBSe alloy film was prepared in one step by simultaneous electrodeposition from 80 ml solution containing 50 mM Cu(NO<sub>3</sub>)<sub>2</sub>·3H<sub>2</sub>O + 50 mM Bi(NO<sub>3</sub>)<sub>3</sub>·5H<sub>2</sub>O + 100 mM SeO<sub>2</sub>. About 10 ml 0.5 M NH<sub>4</sub>NO<sub>3</sub> was added as a stabilizing agent, while 2 ml conc. nitric acid was also added to the solution to ensure the complete solubility of salts by adjusting the pH at 3. The obtained films were rinsed with deionized water, absolute ethanol, and put in a vacuum drying oven

(Nabertherm, NAB 8122) at 50 °C for 6 h. Finally, both successively and simultaneously deposited films were annealed at 300 °C in inert gas of (Ar/H<sub>2</sub> 5%) for one hour.

### 2.3 Characterization techniques

The prepared films were characterized using X-ray diffraction (XRD), Bruker advanced D8 Kristalloflex (Ni-filtered Cu K $\alpha$ <sub>1</sub> radiation; 1.5406 Å) for detecting the crystal structure. The surface characteristics of the deposited film were envisaged through field emission scanning electron microscope (FESEM) Model INSPECT S50, which integrated with built-in units for energy-dispersive X-ray spectroscopy analysis (EDX) and elemental mapping. XPS spectra for CBSe film were measured using X-ray Photoelectron Spectrometer (Thermo Scientific, Model: K-Alpha surface analysis) equipped with a monochromatic small-spot XPS system to scan spectra in the range of 0–1000 eV using Al-K $\alpha$  source and calibrated by C 1 s line.

### 2.4 Optical and photoelectrochemical characterizations

Optimum deposition parameters were applied to obtain CBSe films on ITO-coated glass for further optical and photoelectrochemical measurements using both successive and simultaneous electrodeposition ways. Optical absorbance was recorded using UV–Vis–NIR spectrophotometer (Perkin Elmer Lambda 1050) with an integrated sphere, Deuterium, Tungsten, and Halogen light sources, and a 3-detector module. Photocurrent–voltage characterization was conducted for photoelectrochemical cell (PEC) in which, CBSe film on ITO glass acted as working electrode versus graphite (C) as the counter electrode in 50 mM KI + 50 mM I<sub>2</sub> solution as conducting and regeneration electrolyte at the power of 1 sun (100 mW/cm<sup>2</sup>). Photoelectrochemical characterization was carried out using solar simulator model Science-Tech SS 150 W- AAA supplied with Xenon arc lamp of power 150 W as the light source.

## 3 Results and discussion

### 3.1 Successive electrodeposition study of CBSe film

#### 3.1.1 Electrodeposition study of Cu-Se binary alloy

LSV curves for the deposition of Cu-Se alloy on Pt substrate were carried at different stirring rates, bath temperature, and scan rates as shown in Fig. 1a–c. Clearly, all voltammograms show two definite deposition peaks at – 0.15 and – 0.39 V, which could be assigned to the deposition of the two existing ions Se<sup>–2</sup> and Cu<sup>+2</sup>, respectively [18]. Moreover, LSV results reveal that the deposition current of cathodic peaks increases with an increase in stirring rate as shown in Fig. 1a. The reason for improving the deposition reaction rate is the enhancement in the diffusion of Cu and Se ions from bulk electrolyte to the surface of platinum substrate resulting in a remarkable increase in the deposited film thickness. Thus, increasing the agitation speed accelerates ions transfer and induces high deposition reaction rates at the substrate surface [21–23]. However, high stirring speed could reduce the current efficiency due to the instability of the deposited films at vigorous dynamic conditions [24]. Thus, the optimum stirring speed for obtaining stable film was fixed at 400 rpm. Diffusion current is also proportional to the concentration gradient according to the following Fick's law relation (Eqs. 1 and 2) [25];

$$\frac{\partial C}{\partial t} = -D \frac{\partial^2 C}{\partial x^2} \quad (1)$$

$$i_d = DnAF \frac{dC}{dx} \quad (2)$$

where “ $i_d$ ” is diffusion-limited current, “ $n$ ” is the number of electrons transferred, “ $F$ ” is the Faraday constant (96,485 C mol<sup>–1</sup>), “ $A$ ” is the area of the substrate, “ $D$ ” is the diffusion coefficient, and ( $dC/dx$ ) is the concentration gradient. Also, raising the bath temperature from 25 to 75 °C increases the ion's mobility in the solution. This leads to higher mass transfer of the ions from the bulk solution to the electrode surface, hence increasing the rate of deposition reaction. However, the deposition at 75 °C was not selected to avoid the partial oxidation of the CBSe [26]; therefore, the deposition temperature was optimized at a moderate value of ~50 °C, Fig. 1b. The effect of diffusion and scan rate on the peak current is governed by the Randles–Sevcik Eqs. (3, 4) [25], which explain that the current density is directly proportional to the diffusion and scan rate. This can be explained by enhancing the mobility of Cu and Se ions which consequently increases the cathodic current and the potential of the cell. In other words, higher scan rates lead to higher polarization resulting in a higher deposition rate [27, 28]. Thereby, higher values of the cathodic current density of about –30 mA cm<sup>–2</sup> could be obtained in a potential range from –0.15 to –0.4 V at the maximum scan rate of 10 mV s<sup>–1</sup> as shown in Fig. 1c:

$$i_p = 0.4463nFAC \sqrt{\frac{nFvD}{RT}} \quad (3)$$

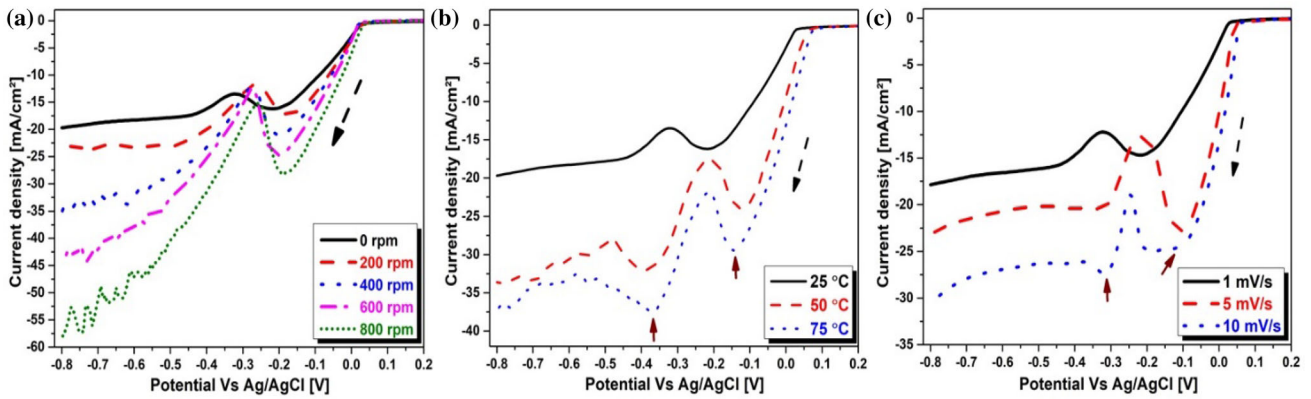


Fig. 1 LSV curves for an aqueous solution of 50 mM Cu(NO<sub>3</sub>)<sub>2</sub>·3H<sub>2</sub>O + 100 mM SeO<sub>2</sub> at different: a stirring rates, b bath temperatures, and c scan rates

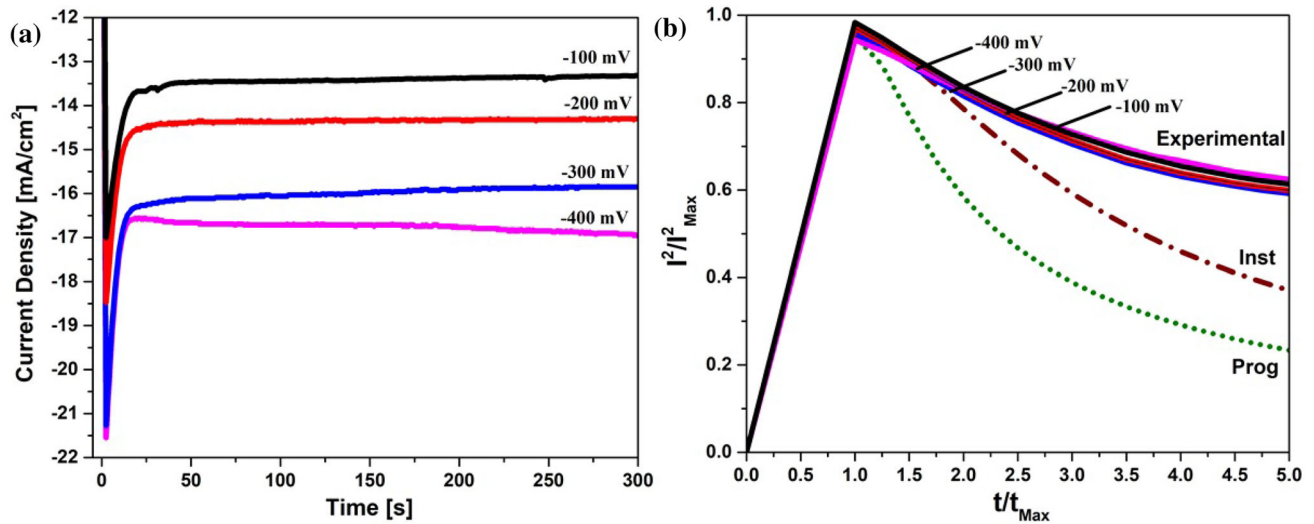


Fig. 2 a Potentiostatic curves of Cu-Se alloy deposition at various electrode potentials, b Corresponding plots for the S–H model

At 25 °C it will be:

$$i_p = (2.69 \times 10^5) n^{3/2} A D^{1/2} v^{1/2} C \tag{4}$$

where “*i<sub>p</sub>*” is the peak current, “*n*” is the number of electrons sharing in the reaction, “*A*” is the active surface area of the working electrode (cm<sup>2</sup>), “*D*” is the diffusion coefficient of active ions in the solution (cm<sup>2</sup> s<sup>-1</sup>), “*v*” is the scan rate (V s<sup>-1</sup>), and “*C*” is the molar concentration (mol cm<sup>-3</sup>). As a result, the current density ranging from 0 to – 40 mA cm<sup>-2</sup> is suitable for the deposition of Cu-Se alloy, where the proper deposition potential is ranged from 0 to – 400 mV values. Thus, the binary alloy is preferably electrodeposited at – 400 mV to avoid the deposition of separate elements.

Figure 2a reveals the potentiostatic curves for the electrodeposition of Cu-Se alloy from an aqueous solution of 50 mM Cu(NO<sub>3</sub>)<sub>2</sub>·3H<sub>2</sub>O + 100 mM SeO<sub>2</sub> at 25 °C at constant potential values -100, -200, -300, and -400 mV. The observed results demonstrate that the current density increases rapidly to its maximum value (*I<sub>max</sub>* and *t<sub>max</sub>*), considering a higher rate of initial deposition reaction, then decreases gradually with time due to double-layer charging. Thereby, approaching the steady state is controlled by the diffusion of ions from the bulk solution to the electrode surface. Furthermore, *I<sub>max</sub>* increases and *t<sub>max</sub>* decreases with increasing the applied potential [29–31]. Basically, the steady state of electrodeposition is governed by Fick’s first law of diffusion, which indicates that the diffusion flux “*J*” is proportional to the concentration gradient as given by Eq. (5) [25]:

$$J = -D \frac{\partial C}{\partial x} \tag{5}$$

where “*D*” is the diffusion coefficient (cm<sup>2</sup> s<sup>-1</sup>), the negative sign indicates the direction of flow from high concentration to low concentration and “*dC/dx*” is the concentration gradient that is the driving force for the steady-state predomination.

Based on Scharifker and Hills model, the nucleation mechanisms for electrodeposition reactions can be studied. Two different equations have been derived to determine the nucleation-growth mechanism simply known as the S–H model [32, 33]. By applying

this model, two mechanisms are limiting the nucleation-growth process, namely the instantaneous and progressive nucleations. The instantaneous nucleation occurs when all nuclei are immediately formed after applying a potential step. Meanwhile, progressive nucleation is caused by the gradual increase in nuclei numbers with the deposition time [32]. The S–H model equations are based on mass transfer that limits the current density for these two types of growth mechanisms and identified as follows: -

Instantaneous nucleation:

$$(i/i_{max})^2 = \frac{1.9542}{(t/t_{max})} \{1 - \exp[-1.2564(t/t_{max})]\} \tag{6}$$

Progressive nucleation:

$$(i/i_m)^2 = \frac{1.2254}{(t/t_{max})} \{1 - \exp[-2.3367(t/t_{max})^2]\}^2 \tag{7}$$

where “ $i_{max}$ ” and “ $t_{max}$ ” are corresponding to the maximum current and its maximum time, respectively. The S–H model is applied based on the potentiostatic studies, and the deposition mechanisms were discussed for the first 5 s of each deposition process. The calculated theoretical and experimental S–H models for the obtained data are presented in Fig. 2b. The plotted curves indicate that the electrochemical deposition reactions proceeded through an instantaneous nucleation mechanism.

Usually, the deposition reactions occur alongside reactions, which are defined as faradic and non-faradic processes, respectively. Side reactions include adsorption, desorption of active species, hydrogen, oxygen evolution, and water dissociation, which consume part of the applied potential and current density. Hence, it is essential to calculate the current efficiency to identify the ratio of the current devoted to the main electrodeposition reaction that serves to form the target films. The ratio between the partial current of the main process of interest and the overall applied current is the current efficiency (CE) percentage [34]. Theoretical weight can be calculated from the first law of Faraday for electrodeposition and substituting in Eq. (8):

$$Current\ Efficiency(CE) = \left[ \frac{W_{Act}}{W_{Theo}} * 100 \right] = \frac{\Delta m}{(QM/nF)} \tag{8}$$

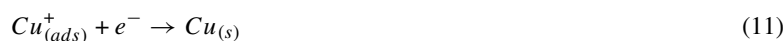
where “ $W_{act}$ ” is the actual practical weight of metal deposited, calculated by weighing the working electrode before and after deposition, and “ $W_{theo}$ ” is the theoretical weight expected from Faraday’s laws if there is no side reaction. “ $\Delta m$ ” is the mass of deposited metal (grams), “ $Q$ ” is the total charges passing through the circuit (coulombs) and “ $M$ ” is the atomic weight of deposited metal or alloy compound. Film thickness “ $t$ ” can be calculated using formula (9) [18];

$$film\ thickness(t) = \frac{\Delta m}{(A * \rho)} \tag{9}$$

where “ $\rho$ ” is the density of the deposited metal or alloy compound ( $g.cm^{-3}$ ), assigned from the obtained phase in XRD pattern and “ $A$ ” is the area of the deposited film ( $2\ cm^2$ ). Meanwhile, the galvanostatic electrodeposition of Cu-Se binary alloy from an aqueous solution of 50 mM  $Cu(NO_3)_2 \cdot 3H_2O$  + 100 mM  $SeO_2$  at 25 °C can be systematically studied at different current densities ranging from – 10 to – 40  $mA.cm^{-2}$  as shown in Fig. 3a. The observed chronopotentiometry curves demonstrate that the deposition potential sharply increases in the first few seconds due to the electrodeposition of the ions surrounding the electrode surface and after that, it is slightly decreased until it reaches the maximum constant values (i.e., steady state) as a result of crystallization step with high dense film thickness.

Figure 3b represents the current efficiency and film thickness variation with the applied current density. It can be noticed that the maximum current efficiency value of about 84% can be achieved in the current density range of – 30 to – 50  $mA.cm^{-2}$ . This value of current efficiency provides the most stable Cu-Se film with a thickness of about 4  $\mu m$ .

Normally, the deposition process proceeds through different primary proposed reactions from (10) to (14) concluded from the XRD and XPS, and EDS analysis as follows:



### 3.1.2 Structural and morphological characterization of deposited Cu-Se film

Figure 4a shows the XRD pattern with the corresponding Miller indices for galvanostatically electrodeposited binary Cu-Se alloy at a value of current density—40  $mA.cm^{-2}$ , 400 rpm, and 50 °C. The diffraction peaks indicate the formation of  $Cu_3Se_2$  as major

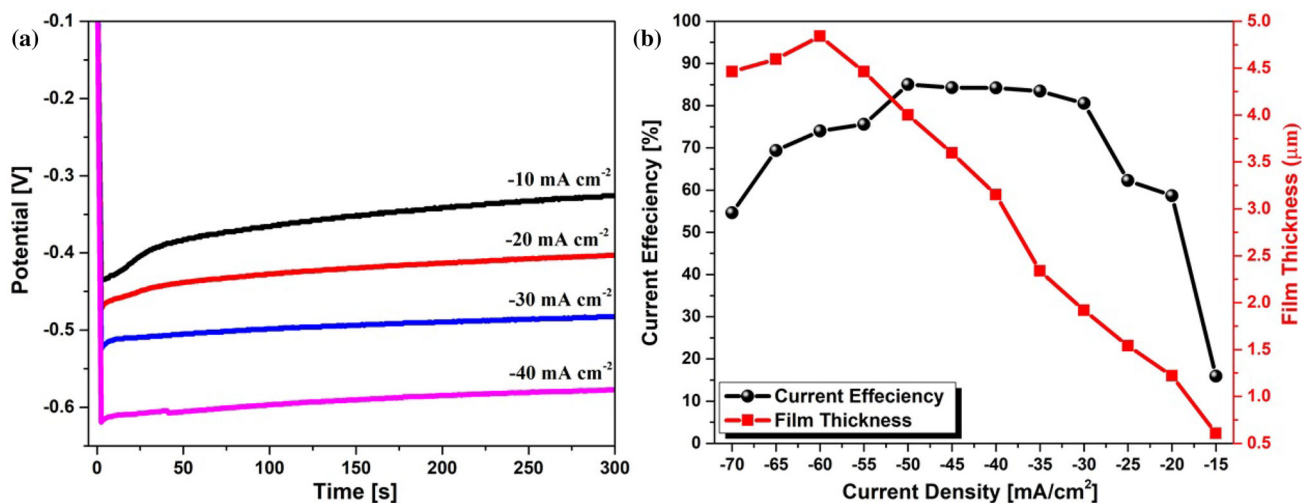


**Fig. 3** **a** Galvanostatic curves for electrodeposition of Cu-Se at various current densities, **b** Current efficiency and film thickness variation with current density

phase with the tetragonal crystal structure (JCPDS # 01–072-1421) [34]. In addition, a minor phase of CuSe alloy that matching the reference card (JCPDS#034–0171) was noticed as small peaks in the XRD pattern. Furthermore, peaks at  $2\theta = 39.7$ ,  $46.2$ , and  $67.5$  correspond to the Pt substrate. Figure 4b and c depicts the SEM images of Cu-Se film at two magnifications 4000 and 10,000 X. The morphology of Cu-Se alloy appears as nano-clusters with a homogeneous sphere-like shape with a particle size of about 500 nm. This formed film of Cu-Se alloy coat contains many voids and spaces between the particles, which enable good adhesion properties for further electrodeposition of Bi metal. EDX analysis, Fig. 4d, indicates that the two elements Cu and Se are very close in their weight percentages, suggesting the equilibrium in their deposition rate.

### 3.1.3 Electrodeposition study of Bi on Cu-Se/Pt

Figure 5a shows the chronoamperometric electrodeposition curves of Bi on the previously deposited Cu-Se/Pt substrate from an aqueous solution of 50 mM  $\text{Bi}(\text{NO}_3)_3 \cdot 5\text{H}_2\text{O}$  at 25 °C using different applied potentials from  $-50$  to  $-200$  mV. Electrodeposition process for the ternary alloy increases in the negative value with increasing the applied potential. For each deposition curve, the current density quickly increases during the first five seconds till reaching its maximum value, then starts to gradually decrease with time. Thereafter, the current density increases again above passing 30 s till it reaches the steady state. Such deposition process is controlled by diffusion of  $\text{Bi}^{3+}$  ions from the bulk solution to the rough substrate surface of Cu-Se alloy. The kinetics and nucleation mechanism can be predicted from the calculated and experimental S–H models for the chronoamperometric data. Therefore, the current–time plots in Fig. 5b indicate that the deposition reaction obeys the instantaneous nucleation mechanism. Typically, the deposition process proceeds through different reactions with the proposed Eqs. (15) and (16) as follows:

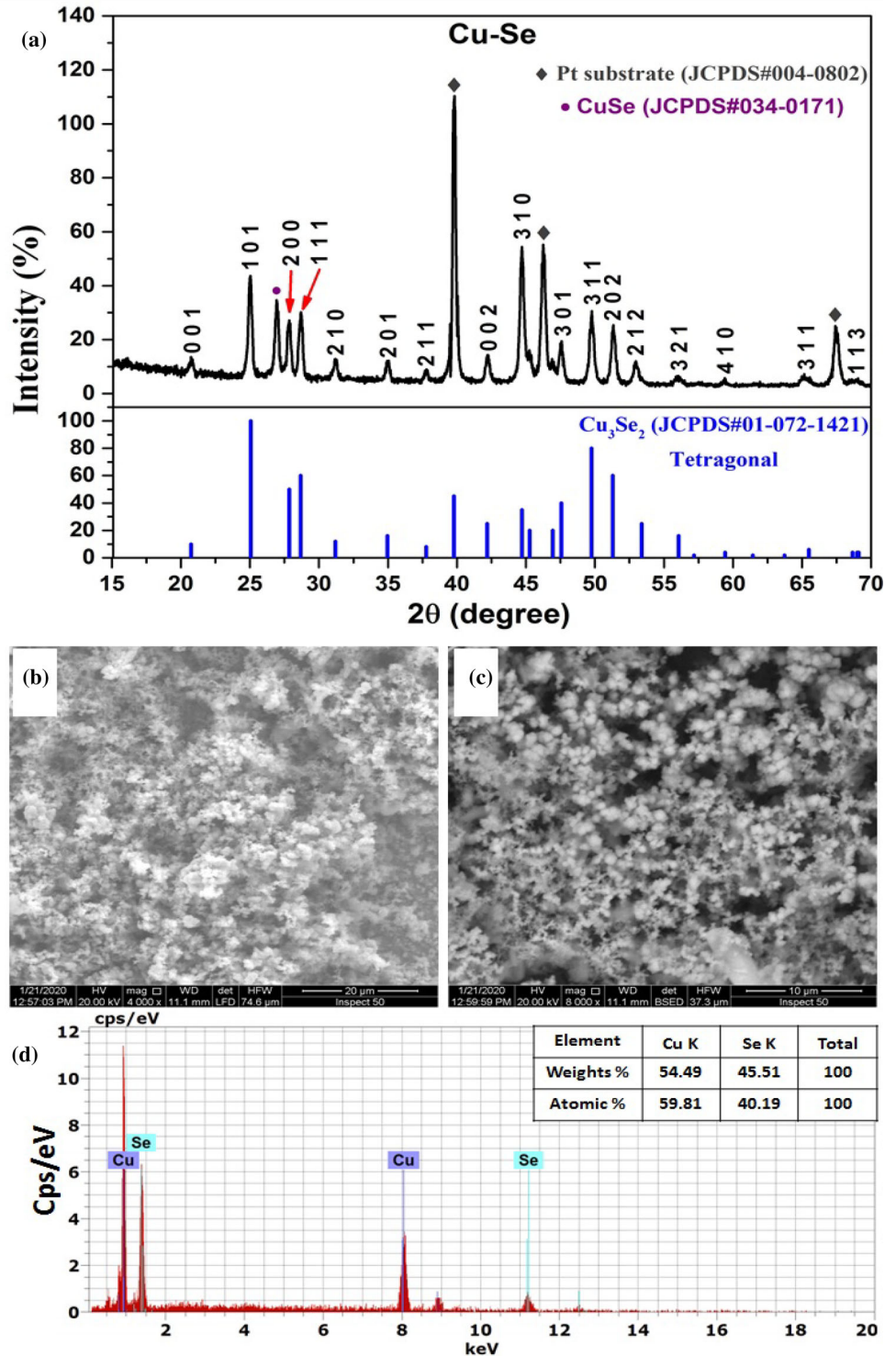


Galvanostatic electrodeposition curves of Bi on Cu-Se/Pt from an aqueous solution of 50 mM  $\text{Bi}(\text{NO}_3)_3 \cdot 5\text{H}_2\text{O}$  at 25 °C at different values of current densities  $-10$ ,  $-20$ ,  $-30$ , and  $-40$  mA·cm<sup>-2</sup> are shown in Fig. 6a. Similarly, the potential is directly proportional to the applied current density in the cathodic direction. This trend reflects the impact of deposition substrate on the behavior of the deposited material [35]. The calculated current efficiency and film thicknesses for galvanostatic electrodeposition of Bi on CuSe/Pt are plotted against current density as displayed in Fig. 6b. The increase in the current efficiency and film thickness values with increasing the current density is discussed by the first law of Faraday discussed before in Eq. (8) [27, 35]. The most stable film with a thickness equal to 2.1 μm was obtained at a current density of  $-40$  mA·cm<sup>-2</sup> with 60% current efficiency. This film was used for further physicochemical characterizations.

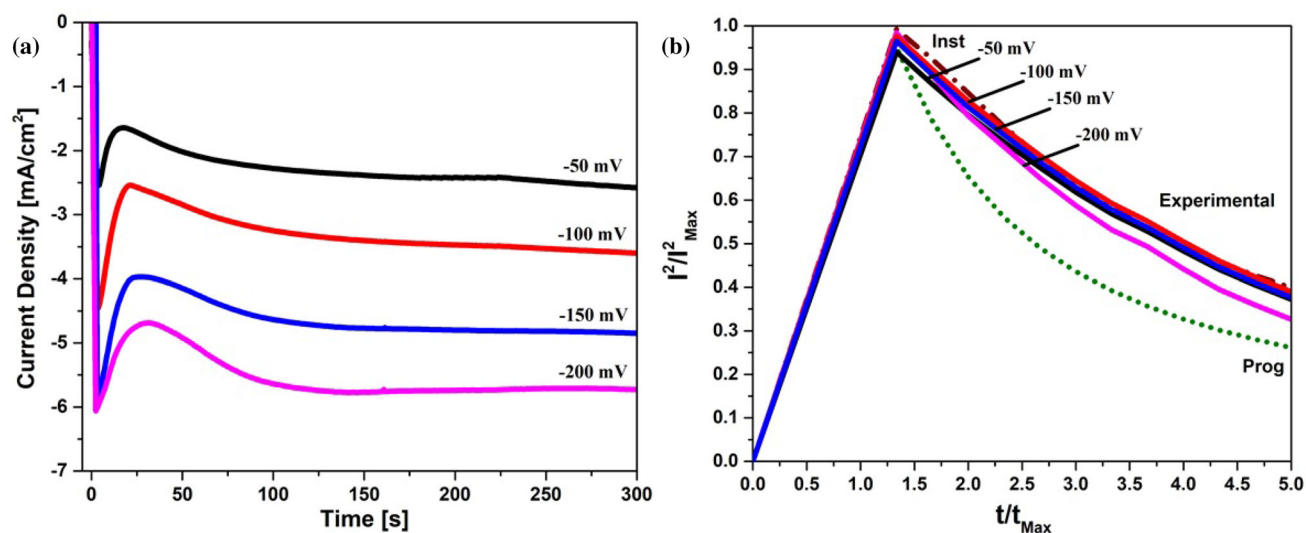
### 3.1.4 Structural and morphological characterization of formed CBSe by successive electrodeposition

Figure 7a depicts the XRD pattern for the deposited CBSe film by successive galvanostatic electrodeposition (i.e., two steps with conditions as mentioned in the experimental part at  $-40$  mA·cm<sup>-2</sup>, 400 pm, and 50 °C). The diffraction peaks indicate the formation of the triclinic polycrystalline  $\text{Cu}_{1.6}\text{Bi}_{4.8}\text{Se}_8$  phase (JCPDS#01-080-1592). The same phase was obtained also with

**Fig. 4** **a** XRD pattern, **b, c** SEM images at different magnifications, **d** EDX analysis for electrodeposited binary Cu-Se alloy



electrodeposition in previously reported work [14]. The formed phase shows high crystallinity suggesting enhanced crystals growth with good orientation. Thus, the successive way for electrodeposition of CuSe film is highly effective and suitable. Some peaks for metallic bismuth with rhombohedral structure in agreement with a reference card (JCPDS#01-085-1329) were observed in the XRD pattern revealing the deposition of elemental Bi during the reaction as a minor phase since the second deposition step in a successive way occurs in a solution of excess Bi<sup>+3</sup> ions. The observed three peaks at 2θ of 39.7°, 46.2°, and 67.5° refer to the presence of platinum substrate with a reference card (JCPDS#004–0802) [36].



**Fig. 5** **a** Potentiostatic curves for electrodeposition of Bi on Cu-Se/Pt at various potentials, **b** Corresponding plots for the S–H model

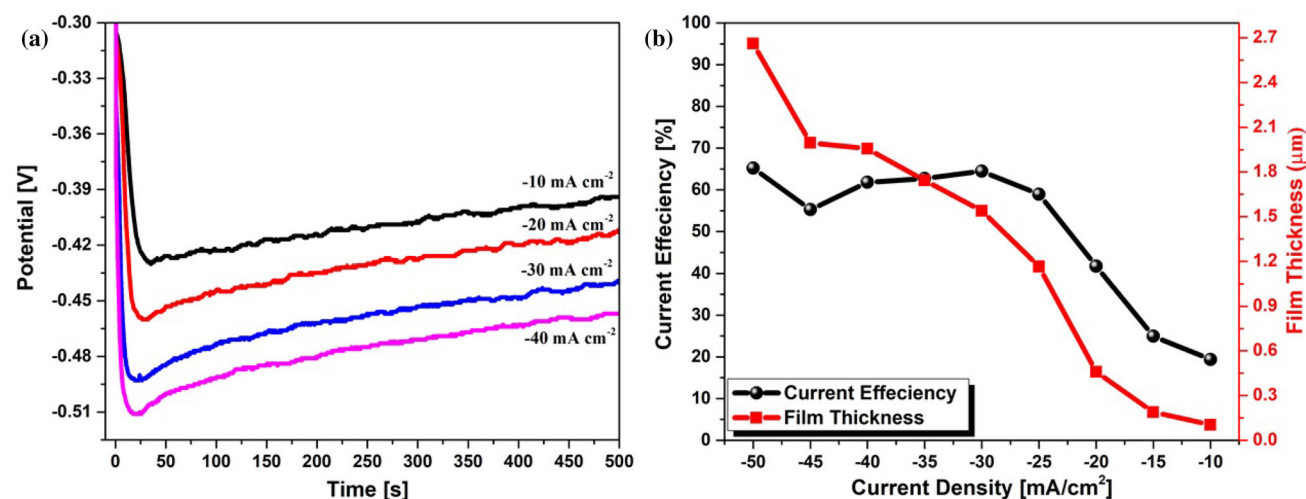


**Fig. 6** **a** Galvanostatic curves for electrodeposition of Bi on Cu-Se/Pt (Successive) recorded at various current densities, **b** Current efficiency and film thickness variation with current density

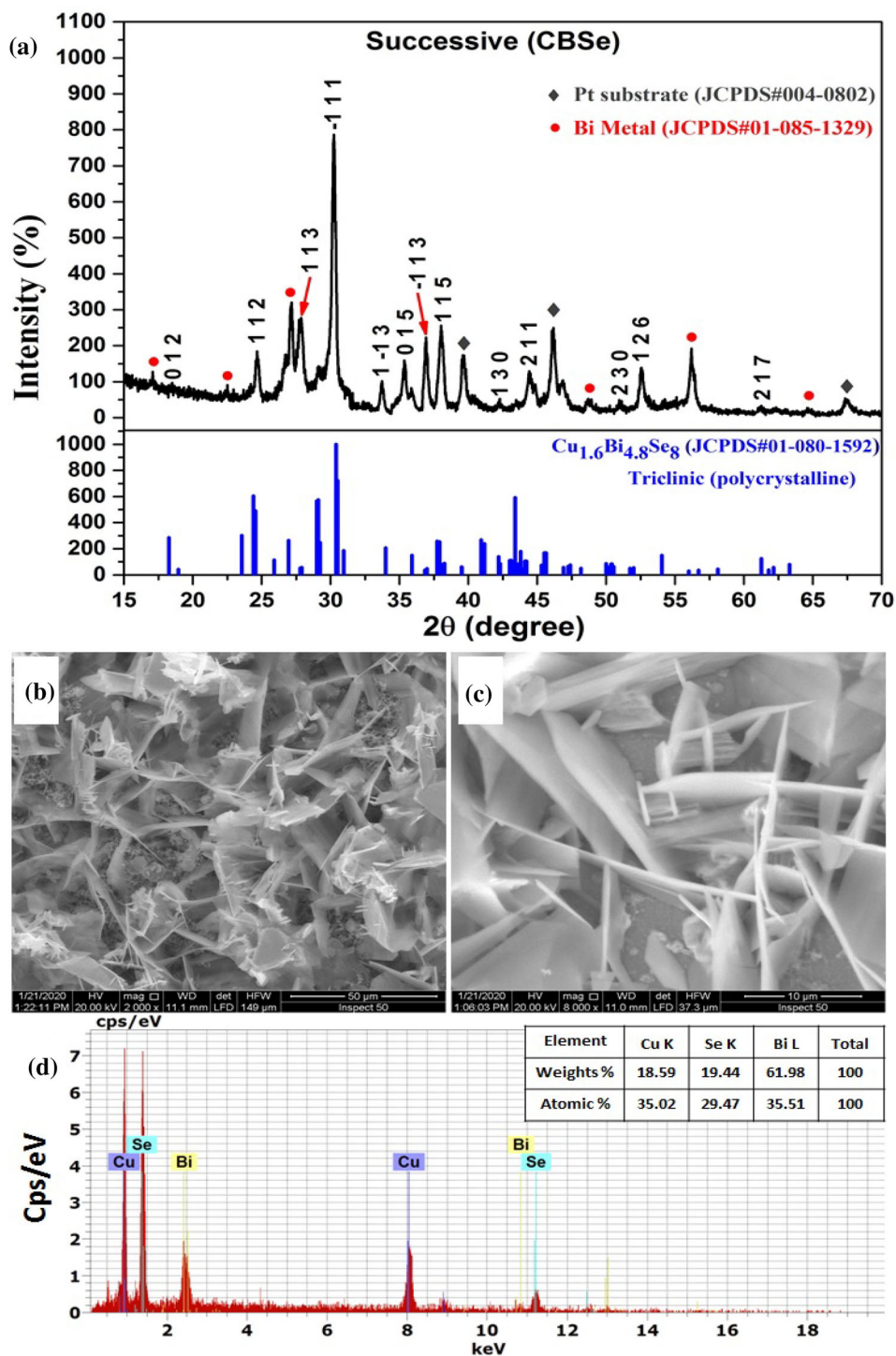
Figure 7b and c depicts the SEM images for formed CBSe film by successive electrodeposition for two different magnifications 2000 and 8000 X. The deposited CBSe film consists of cross-linking hexagonal plates of maze-like shape. These hexagonal interrelated plates are perpendicular to the primary Pt substrate and have a large diameter range of 10–50  $\mu\text{m}$ . EDX analysis in Fig. 7d confirms the presence of the three-component elements Cu, Bi, and Se with non-stoichiometric ratios. The detected Bi in EDX results is consistent with the XRD finding.

Figure 8 displays the elemental mapping of the recorded backscattered electrons for the ternary CBSe alloy formed through successive electrodeposition. The SEM mapping evinces the equal distribution of the three elements Cu, Bi, and Se over the whole sample suggesting the homogeneity of the deposited film [37].

Figure 9a–c indicates the XPS charts of each element Cu, Bi, and Se in the electrodeposited CBSe film through the successive way. Figure 9a displays the XPS scan for copper which consists of two apparent peaks related to  $2P_{3/2}$  and  $2P_{1/2}$  orbitals at 933 and 953 eV, respectively, indicating the presence of  $\text{Cu}^{1+}$  (Cuprous) electronic state [38, 39]. Moreover, the other two peaks at 936.5 and 956 eV for  $2P_{3/2}$  and  $2P_{1/2}$  are corresponding to the  $\text{Cu}^{2+}$  (Cupric) electronic state [40]. Meanwhile, the XPS scan for bismuth confirms the presence of two different oxidation states for Bi. The first peak at 158 eV indicates the presence of metallic Bi, i.e., zero oxidation state, as illustrated from the Bi 4f XPS spectra matching the XRD results [41]. Another two peaks are detected at 160 and 164 eV for  $4f_{7/2}$  and  $4f_{5/2}$  splitting orbitals, respectively, confirming the presence of  $\text{Bi}^{3+}$  oxidation state as depicted in Fig. 9b [40]. Figure 9c reveals the fitting for XPS Scan for 3d Se which shows a peak at 53.7 eV due to the existence of the reduced  $\text{Se}^{2-}$  electronic state [38]. The second peak at 59.5 eV for the orbital  $3d_{3/2}$  could be attributed to the oxidized form of tetravalent  $\text{Se}^{4+}$  [42].



**Fig. 7** **a** XRD pattern, **b, c** SEM images at different magnifications, and **d** EDX analysis for successive electrodeposited ternary CBSe film

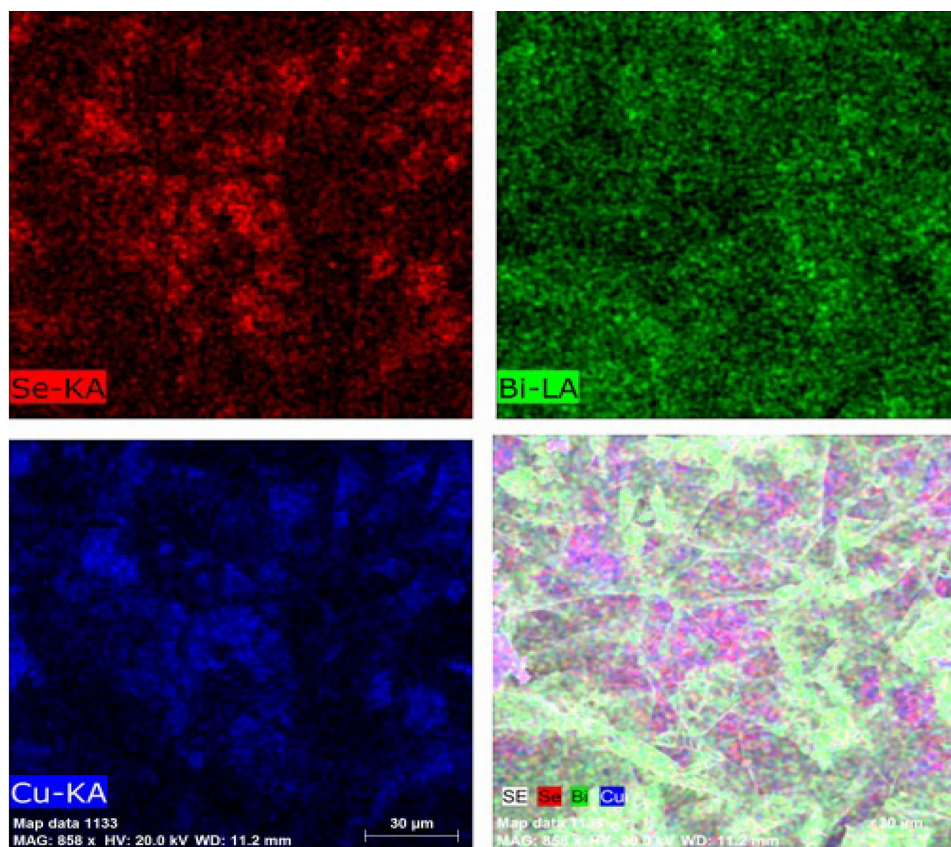


### 3.2 Simultaneous electrodeposition of ternary CBSe alloy

#### 3.2.1 Electrodeposition study of ternary CBSe alloy

Figure 10a–c reveals the LSV curves for CBSe deposition from solution mixture: 50 mM Cu(NO<sub>3</sub>)<sub>2</sub>·3H<sub>2</sub>O + 50 mM Bi(NO<sub>3</sub>)<sub>3</sub>·5H<sub>2</sub>O + 100 mM SeO<sub>2</sub> in potential range – 1.0 to 0.25 V. It is obvious that the enhancement of deposition rate occurs with increasing stirring speed up to 400 rpm, bath temperature up to 75 °C and the scan rate up to 10 mVs<sup>-1</sup>. This could be explained by the diffusion factor, which is enhanced by stirring resulting in increasing the rate of deposition reaction and obtaining a higher current density. Also, the presence of three cathodic peaks at – 0.16, – 0.34, and – 0.74 V during LSV without agitation could be attributed to the

**Fig. 8** Elemental mapping results for the successive electrodeposited CBSe film



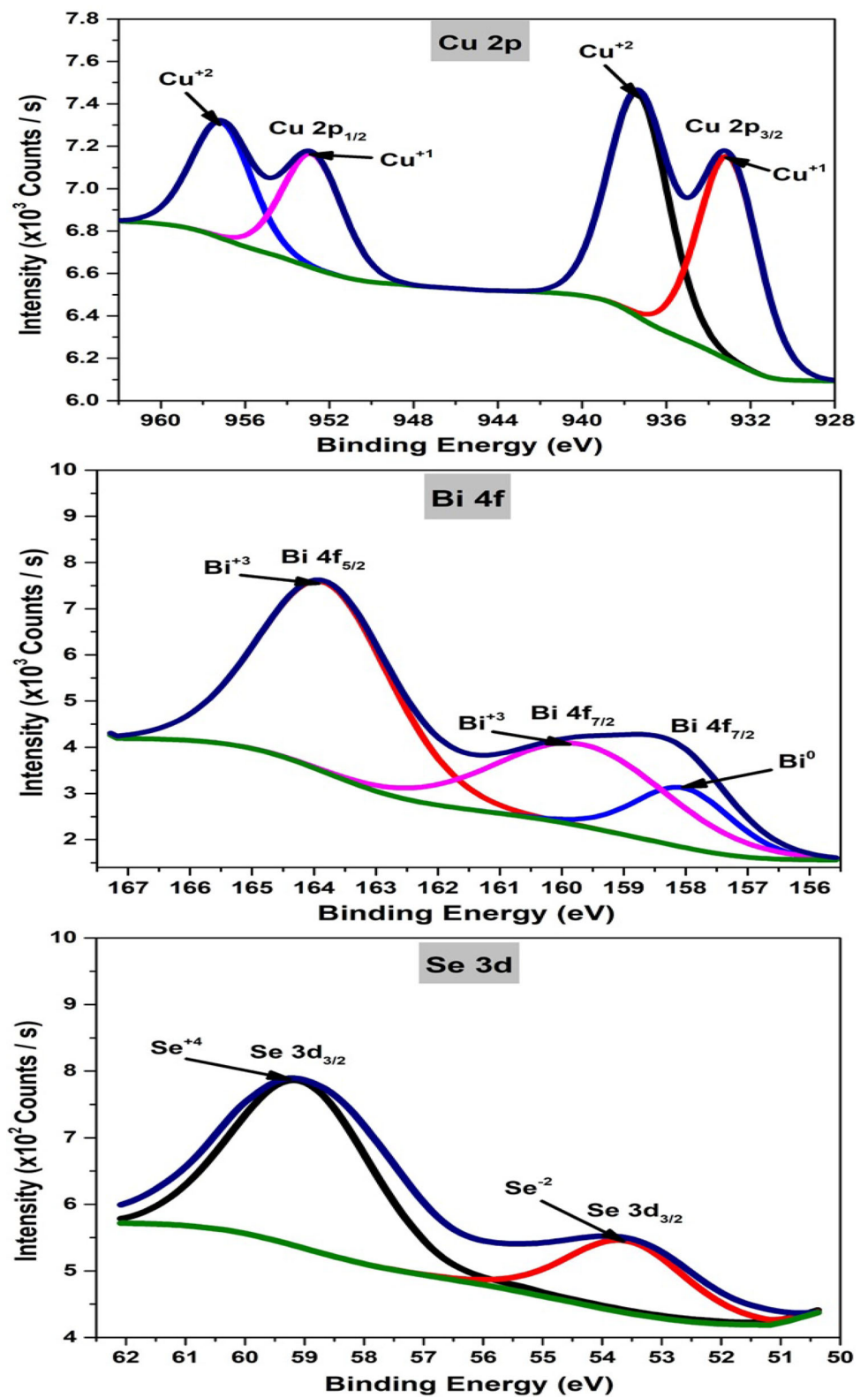
deposition of Se, Cu, and Bi ions, respectively [14]. Likely, the suitable conditions for obtaining a higher current density for CBSe deposition are 400 rpm, 50 °C, and 10 mV/s.

Figure 11a shows the chronoamperometric curves for the simultaneous electrodeposition of ternary CBSe alloy from a solution mixture of 50 mM Cu(NO<sub>3</sub>)<sub>2</sub>·3H<sub>2</sub>O + 50 mM Bi(NO<sub>3</sub>)<sub>3</sub>·5H<sub>2</sub>O + 100 mM SeO<sub>2</sub> at different applied potentials – 100, – 200, – 300, and – 400 mV. The observed behavior of increasing the deposition rate of ternary elements (CuBiSe@Pt) with increasing applied deposition potential is similar to that of binary (CuSe@Pt) and ternary (Bi@Cu-Se@Pt) elements obtained by successive electrodeposition process. Moreover, the deposition curves can be distinguished into two different parts, the first one includes rapid deposition with high current density within a few seconds (<5 s). The second part comes from the slow deposition rate due to the grain growth and film propagation till approaching the steady state, which is governed by the diffusion process of the ions from the bulk solution to the electrode surface [27]. The kinetic behavior of the deposition reactions is also studied through the (S–H) model, which was calculated from the potentiostatic data as displayed in Fig. 11b. The deposition process shifted toward the progressive nucleation deposition mechanism.

Figure 12a demonstrates the chronopotentiometry diagrams for the galvanostatic electrodeposition of CBSe from aqueous solution containing 50 mM Cu(NO<sub>3</sub>)<sub>2</sub>·3H<sub>2</sub>O + 50 mM Bi(NO<sub>3</sub>)<sub>3</sub>·5H<sub>2</sub>O + 100 mM SeO<sub>2</sub> at different current densities ranging from – 10 to – 40 mA cm<sup>–2</sup>. Principally, the potential is increased with increasing the applied current density. By applying current density, a sharp increase in the potential was noticed in the negative direction to the maximum value. With passing the deposition time, the potential slightly decreases till it reaches the steady state, which depends on the diffusion process of ions from bulk to the electrode surface. The current efficiencies and film thicknesses of the deposited films can be calculated between the current density range from – 20 to – 90 mAcm<sup>–2</sup> as displayed in Fig. 12b. The most stable and dense CBSe film can be obtained at a current density – 50 mAcm<sup>–2</sup>, which gives the highest current efficiency of ~70% and film thickness of about 1.58 μm. This film was used for further characterization, i.e., XRD, SEM, EDS, and conditions were applied for the electrodeposition on ITO glass for optical and photoelectrochemical characteristics. The simultaneous electrodeposition process occurs through different reactions according to the proposed equations from (17) to (25):



**Fig. 9** XPS charts for elemental components **a** Cu, **b** Bi, and **c** Se of the successively electrodeposited CBSe ternary phase



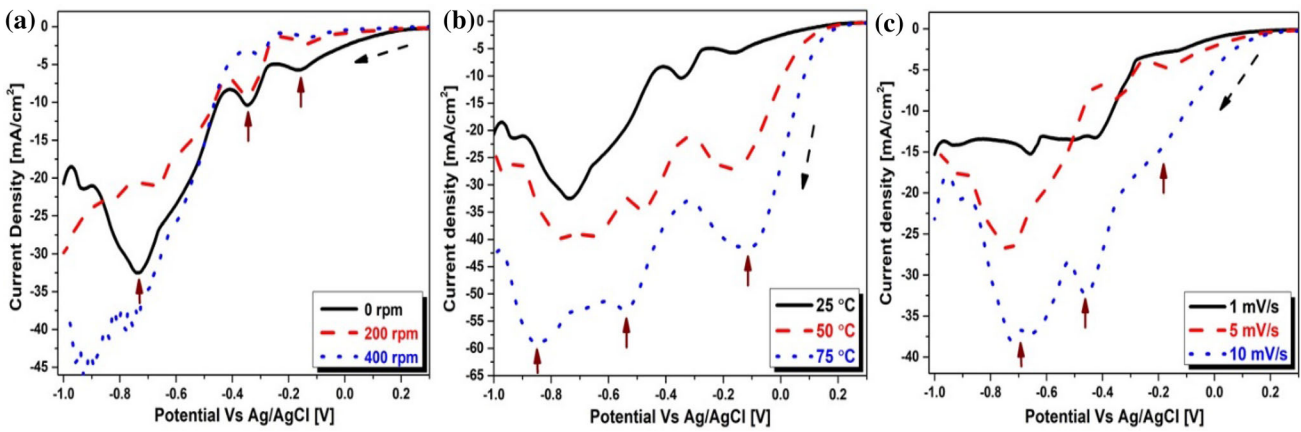


Fig. 10 LSV for simultaneous electrodeposition of CBSe alloy at different, a stirring rates, b bath temperatures, and c scan rates

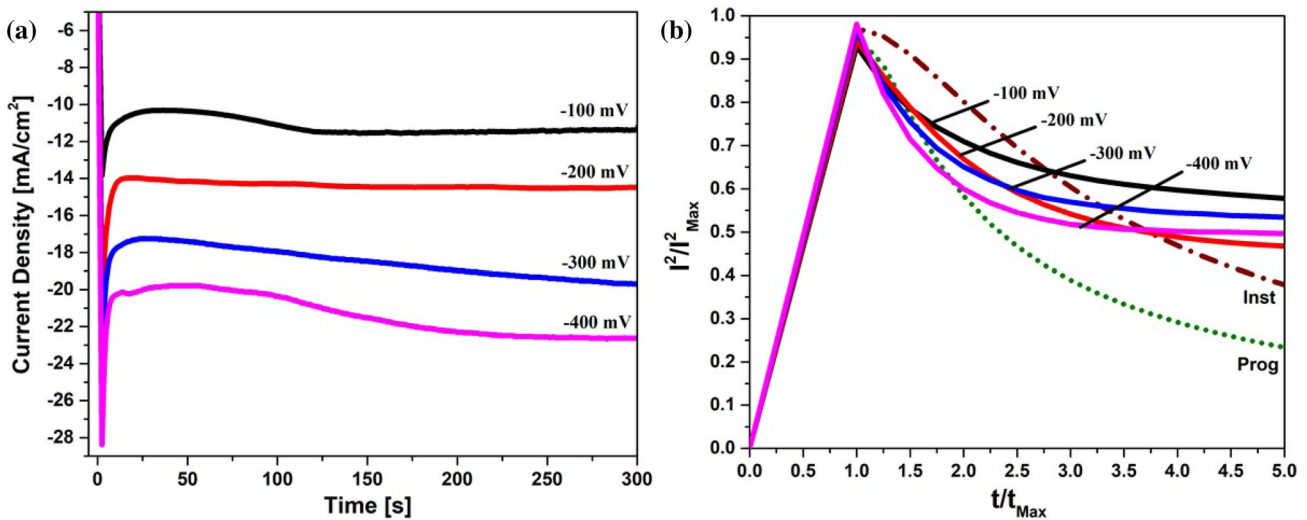
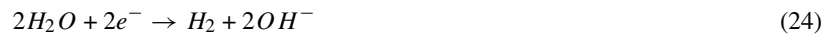
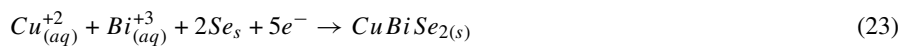
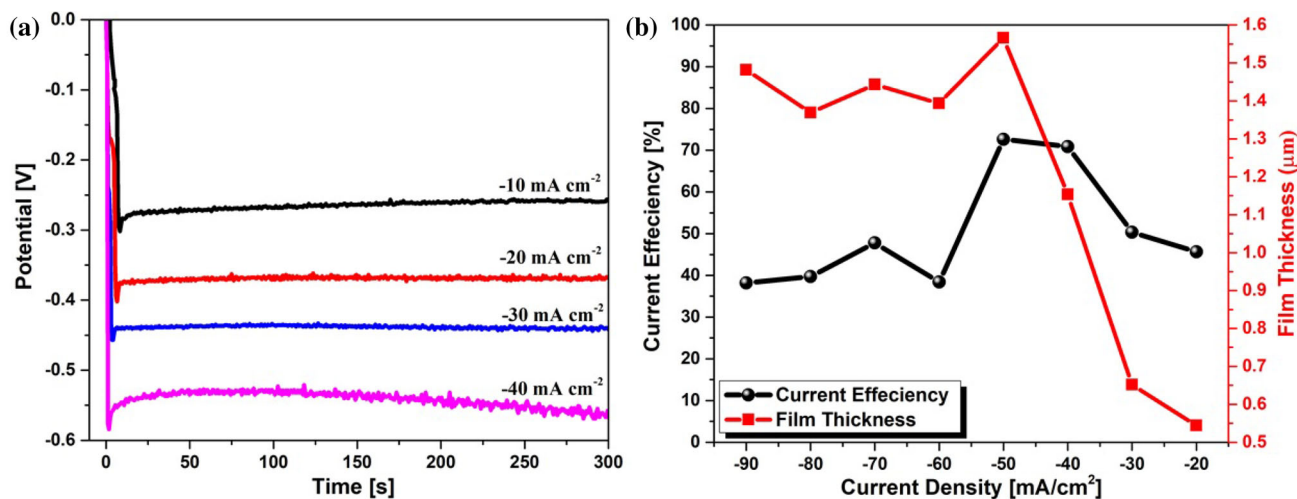


Fig. 11 a Potentiostatic curves of simultaneous electrodeposition of CBSe deposition at various electrode potentials from aqueous solution of 50 mM  $Cu(NO_3)_2 \cdot 3H_2O$  + 50 mM  $Bi(NO_3)_3 \cdot 5H_2O$  + 100 mM  $SeO_2$  at 25 °C, b Corresponding plots for the S-H model



### 3.2.2 Structural and morphological characterization of simultaneous electrodeposited CBSe

Figure 13a represents the XRD pattern for the deposited CBSe film by simultaneous electrodeposition (i.e., one step at  $-40 \text{ mA cm}^{-2}$ , 400 rpm, 50 °C). The observed diffraction peaks are related to the same ternary polycrystalline  $Cu_{1.6}Bi_{4.8}Se_8$  phase as previously detected in successive electrodeposition studies. However, the crystallinity of the formed CBSe film is lower than that of the same CBSe film obtained by successive electrodeposition. This might be attributed to the fast deposition rate and the instantaneous nucleation mechanism resulting in smaller grain size crystals. Moreover, the presence of the three ions in a simultaneous electrodeposition process makes them compete with each other in the deposition on the substrate surface. Thus, the electrodeposition process is difficult to form the ternary alloy with a definite desired stoichiometric ratio [17]. Furthermore, a minor phase of metallic bismuth was also noticed revealing the separate behavior of each ion in the ionic mixture that led to the electrodeposition of metallic bismuth lonely instead of combining with the other ions to form the ternary CBSe alloy.



**Fig. 12** **a** Galvanostatic curves for simultaneous electrodeposited CBSe at various current densities, **b** Current efficiency and film thickness variation with current density

The SEM images for the electrodeposited CBSe film by the simultaneous way are shown in Fig. 13b and c with two magnifications 5000 and 10000X. The morphology of deposited CBSe film appears as semi-hexagonal separated sheets with a diameter range of 10–20 μm. The chemical composition of the CBSe deposited film by EDX analysis in Fig. 13d confirms the close presence of the Cu and Se, while the Bi exists with a smaller percentage, which shows a lower degree of consistency with XRD results. This could be explained by the presence of certain elements like Bi in the amorphous form. Such obtained results reveal the significance and excellence of the successive electrodeposition of CBSe material rather than the simultaneous one.

### 3.3 Optical properties

The optimum conditions were applied for simultaneous and successive electrodeposition of CBSe films on indium tin oxide-coated glass (ITO glass) to measure the optical absorbance for deposited films. Thereby, deposited films on both Pt and ITO-coated glass using simultaneous and successive electrodeposition are shown in Fig. 14a–d.

Figure 15a shows the absorption spectra for the deposited CBSe films by successive and simultaneous electrodeposition. Although both films absorb light in a wide range of wavelengths of UV–Visible light, the CBSe film obtained by successive method reveals higher absorbance intensity than that obtained by the simultaneous way as a result of ordered structure. By applying Tauc's law of Eq. (26), the bandgap energy values of the deposited CBSe films can be calculated from the linear extrapolation of the plot relation  $h\nu$  versus  $(\alpha h\nu)^2$  [43].

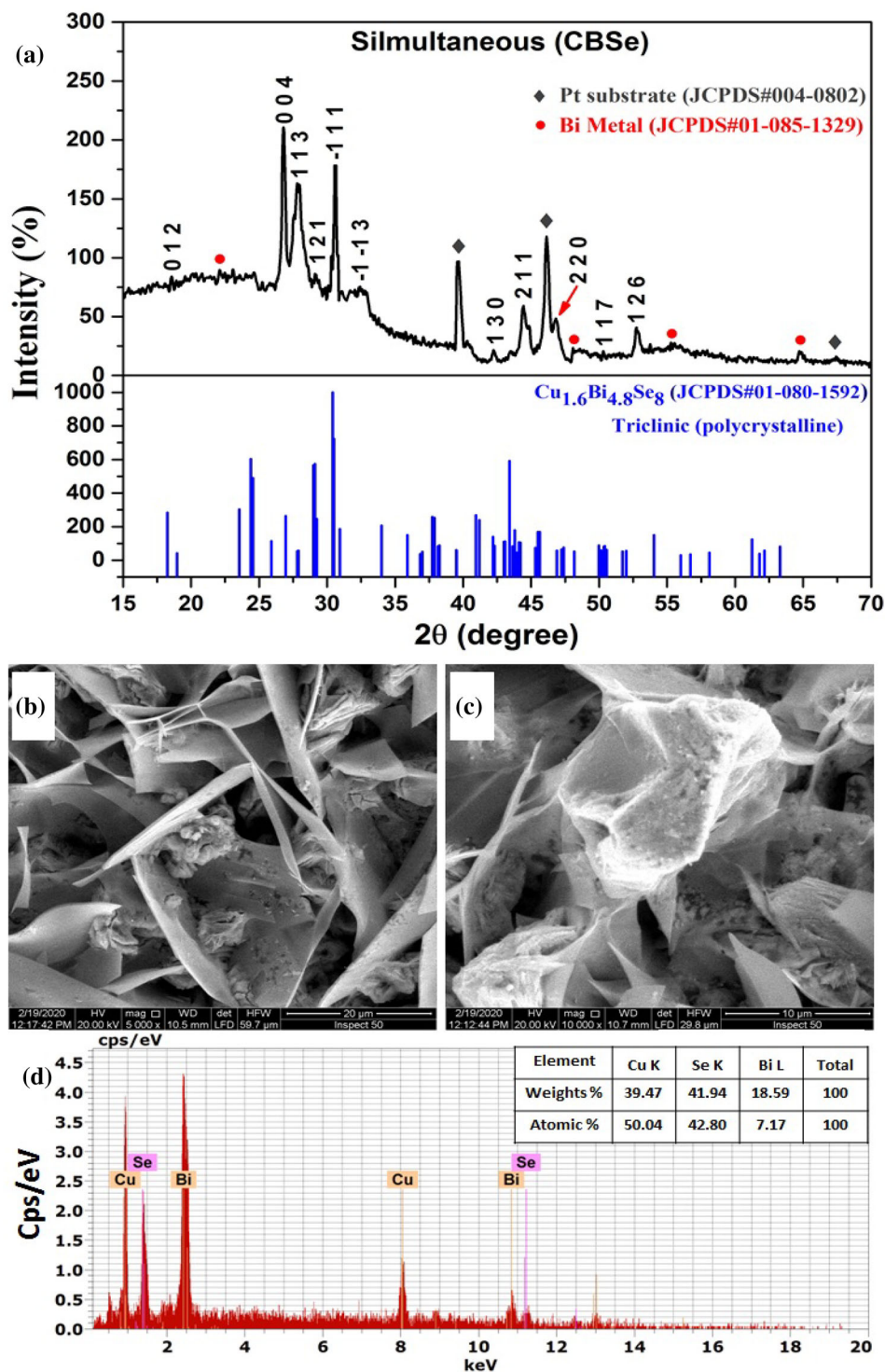
$$\alpha h\nu = A(h\nu - E_g)^{1/2} \quad (26)$$

where “ $\alpha$ ” is the optical absorption coefficient, “ $h$ ” is Planck's constant, “ $\nu$ ” is the photon frequency, “ $A$ ” is a constant, and “ $E_g$ ” is the energy gap. The bandgap of CBSe film obtained by successive electrodeposition, 1.65 eV is lower than that of the film obtained by the simultaneous way: 1.82 eV [15] as shown in Fig. 15b. This could be explained by the fact that the bandgap energy decreases with increasing grain size, crystallinity, and homogeneous morphology [44, 45]. Also, the recorded film thickness for the successively electrodeposited ~6.1 μm is relatively larger than the simultaneously electrodeposited CBSe film ~1.58 μm, which varies inversely with band gap value [46, 47]. The same values of band gaps range (1.67–1.99 eV) were reported for copper bismuth selenide (the same material films) deposited by PVD technique and crystallize in the same phase, i.e., polycrystalline triclinic (Cu<sub>1.6</sub>Bi<sub>4.8</sub>Se<sub>8</sub>) [46, 48]. The band gap for bulk CBSe materials ~0.99 eV prepared by solvothermal process [13] is lower than the obtained values for both electrodeposited CBSe films. In case of thin film materials, the absorption coefficient decreases and thus the refractive index of the optical rays decreases, leading to the increase in the optical band gap relative to bulk materials of thick films [48, 49]. It is essential to note that the material with small bandgap energy can absorb light with a wide range of wavelengths. This allows the maximum utilization of the largest amount of light resulting in a higher photoelectrical response [50]. In general, the obtained band gap energy values are in good agreement with previously reported values for the same material prepared with electrodeposition and other methods [11, 14, 15].

### 3.4 Photoelectrochemical characterization

*I*–*V* characteristic curves of the photoelectrochemical cell (PEC) for electrodeposited CBSe films on ITO-coated glass are shown in Fig. 16. It is obvious that successive electrodeposited CBSe film has higher values of *I*–*V* parameters (e.g., *I*<sub>sc</sub>: short circuit

**Fig. 13** **a** XRD pattern, SEM images, **b** 5000X, **c** 10000X and **d** EDX analysis for simultaneous electrodeposited ternary CBSe alloy



current,  $V_{oc}$ : open-circuit voltage, FF: filling factor) than the simultaneous electrodeposited CBSe alloy. Obviously, the PEC based on successive electrodeposited CBSe anode achieved higher value of power conversion efficiency ( $\eta \sim 1.26\%$ ) than that cell made of successive electrodeposited CBSe anode material ( $\eta \sim 1.1\%$ ). The reason for this improved photoelectrochemical performance could be related to the good crystallinity, uniform microstructure, and high absorptivity of the successively electrodeposited CBSe electrode [51]. However, the obtained  $\eta$  values of PCE for both samples are lower than the previously reported one for the same material prepared by vacuum evaporation and applied as a layer in the stacked solar cell [15]. This behavior occurred, because the photoelectrochemical cell has lower efficiency than the photovoltaic cell as the incident light drops vertically on the cell and not perpendicularly which allows losing of some power. Furthermore, the electrolyte separation is considered as a barrier between the

**Fig. 14** Electrodeposited CBSe films by the two different ways: on Pt substrate, **a** successive, **b** simultaneous, and ITO-coated glass, **c** successive, **d** simultaneous

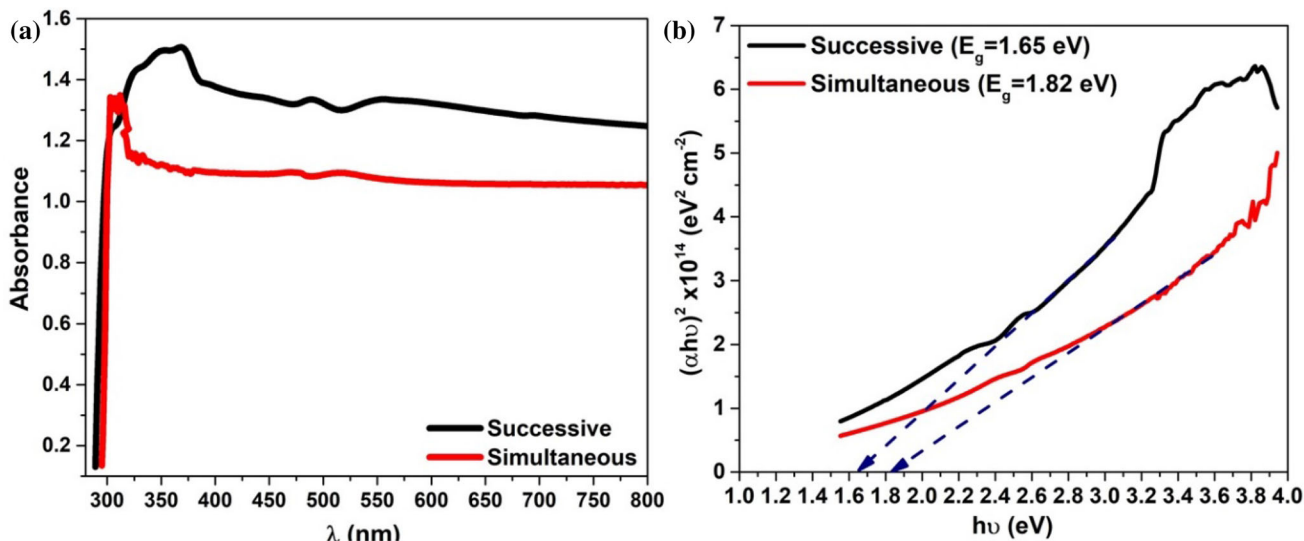
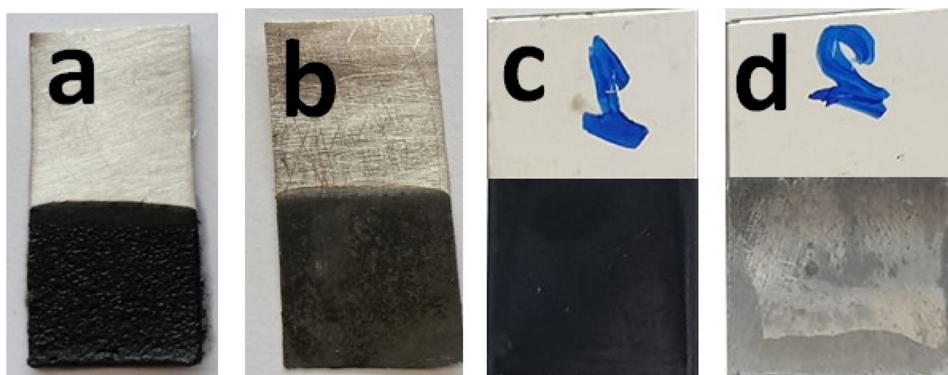
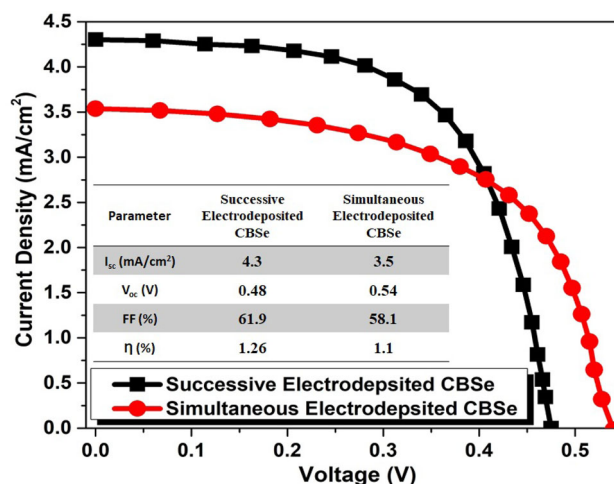


**Fig. 15** **a** Optical absorbance and **b** calculated band gap values for successively and simultaneously electrodeposited CBSe ternary alloy films on ITO-coated glass

**Fig. 16** I–V characteristic curves with its parameters inset for photoelectrochemical cells for successive and simultaneous electrodeposited ternary CBSe on ITO-coated glass



photoanode and the photocathode electrodes that wastes some energy of the incident light, while the photovoltaic has thin films using thinner coats of semiconductors to absorb and convert sunlight directly. The efficiency of CdTe photovoltaic cells is approaching about 20% in the laboratory and recorded at about 22.1% in 2016 [52], while the reported efficiency for CdTe photoelectrochemical cell is about 5% [53]. Therefore, the estimated range of PEC efficiencies for chalcogenide CBSe thin films is in good agreement with the previous studies about thin-film chalcogenides [12, 13].

**Table 1** Overall comparison between the successive and simultaneous electrodeposition ways for CBSe ternary alloy

Comparison items	Successive	Simultaneous
Electrodeposition parameters	Step 1: (Cu-Se) 80 ml solution, pH = 3, $i = -50 \text{ mA}\cdot\text{cm}^{-2}$ , 400 rpm, $10 \text{ mV}\cdot\text{s}^{-1}$ , 25 °C Step 2; (Bi@CuSe) 80 ml solution, pH = 2, $i = -40 \text{ mA}\cdot\text{cm}^{-2}$ , 400 rpm, $10 \text{ mV}\cdot\text{s}^{-1}$ , 25 °C	One step process (Cu-Bi-Se), 80 ml solution, pH = 3, $i = -50 \text{ mA}\cdot\text{cm}^{-2}$ , 400 rpm, $10 \text{ mV}\cdot\text{s}^{-1}$ , 25 °C
Film thickness and corresponding current efficiency (CE)	6.1 $\mu\text{m}$ , CE = 60%	1.58 $\mu\text{m}$ , CE = 70%
Post heat treatment	300 °C/1 h in Ar/H <sub>2</sub> (5%) atmosphere	
Crystallographic parameters of ternary phase	Triclinic polycrystalline Cu <sub>1.6</sub> Bi <sub>4.8</sub> Se <sub>8</sub> (major phase) Bi metal (minor phase)  Crystallinity % = 80	Triclinic polycrystalline Cu <sub>1.6</sub> Bi <sub>4.8</sub> Se <sub>8</sub> (major phase), Bi metal (minor phase)  Crystallinity % = 22
Morphological parameters of ternary phase	Maze-like structure, 10–50 $\mu\text{m}$ diameter	Semi-hexagonal separated sheets, 10–20 $\mu\text{m}$ diameter
Optical band gap (CBSe ITO)	$E_g = 1.65 \text{ eV}$	$E_g = 1.82 \text{ eV}$
I-V characteristics	$I_{sc} = 4.3 \text{ mA}\cdot\text{cm}^{-2}$ , $V_{oc} = 0.48 \text{ V}$ FF = 61.9%, $\eta = 1.26\%$	$I_{sc} = 3.5 \text{ mA}\cdot\text{cm}^{-2}$ , $V_{oc} = 0.54 \text{ V}$ FF = 58.1%, $\eta = 1.10\%$

Summary of the electrodeposition process through the two different successively and simultaneously applied ways is given in Table 1, providing an inclusive comparison between the two ways from where the electrodeposition conditions, studied parameters, and main obtained results.

#### 4 Conclusion

CBSe thin films were successfully electrodeposited on the platinum substrate in two different ways, successive and simultaneous. Different electrodeposition parameters were studied and comprised for the used two paths. XRD patterns for thin films prepared in both ways revealed a triclinic polycrystalline Cu<sub>1.6</sub>Bi<sub>4.8</sub>Se<sub>8</sub> as major phase and Bi metal as minor impurities. The electrodeposited ternary alloy CBSe film prepared by the successive way showed better crystallinity, larger film thickness (~6.1  $\mu\text{m}$ ), and uniform grain morphology. Elemental mapping for the CBSe film deposited by successive way evinced the homogenous distribution of the three elements Cu, Bi, and Se over the whole sample. XPS results for CBSe film by successive electrodeposition indicated that Cu exists in monovalent and divalent states, Bi in the elemental and trivalent states, and Se present in divalent and tetravalent states. The estimated bandgap energy of successive electrodeposited CBSe film offers higher absorption of solar light. Thus, higher power conversion efficiency (PCE) was achieved compared with the simultaneous electrodeposited film. It can be concluded that the successive electrodeposition technique is highly preferred to obtain photo-efficient, highly crystalline and homogeneous thin films of ternary chalcogenide systems.

**Acknowledgements** The authors would like to offer their thanks to the department of indoor projects and programs in CMRDI. These data were supported through indoor projects in CMRDI in 2019 and 2020.

**Funding** Open access funding provided by The Science, Technology & Innovation Funding Authority (STDF) in cooperation with The Egyptian Knowledge Bank (EKB).

**Data availability** All data generated or analyzed during this study are included in this published article.

**Open Access** This article is licensed under a Creative Commons Attribution 4.0 International License, which permits use, sharing, adaptation, distribution and reproduction in any medium or format, as long as you give appropriate credit to the original author(s) and the source, provide a link to the Creative Commons licence, and indicate if changes were made. The images or other third party material in this article are included in the article's Creative Commons licence, unless indicated otherwise in a credit line to the material. If material is not included in the article's Creative Commons licence and your intended use is not permitted by statutory regulation or exceeds the permitted use, you will need to obtain permission directly from the copyright holder. To view a copy of this licence, visit <http://creativecommons.org/licenses/by/4.0/>.



## References

1. J. Britt, C. Ferekides, Thin-film CdS/CdTe solar cell with 15.8% efficiency. *Appl. Phys. Lett.* **62**, 2851–2852 (1993). <https://doi.org/10.1063/1.109629>
2. S. Siebentrit, M. Igalson, C. Persso, S. Lany, The electronic structure of chalcopyrites-bands; point defects and grain boundaries. *Prog. Photovolt.* **18**, 390–410 (2010). <https://doi.org/10.1002/pip.936>
3. D. Hyun, J. Hwang, T. Oh, J. Shim, N. Kolomoets, Electrical properties of the 85% Bi<sub>2</sub>Te<sub>3</sub>-15% Bi<sub>2</sub>Se<sub>3</sub> thermoelectric material doped with SbI<sub>3</sub> and CuBr. *J. Phys. Chem. Solids.* **59**, 1039–1044 (1998). [https://doi.org/10.1016/S0022-3697\(97\)00242-4](https://doi.org/10.1016/S0022-3697(97)00242-4)
4. M.M.S. Sanad, A.Y. Shenouda, Impact of sulphur-containing compounds on the electrochemical capabilities of spinel carbon-coated Sb<sub>2</sub>SnS<sub>4</sub> nano-sheets as alternative anodes in lithium ion batteries. *J. Mater. Sci. Mater. Electron.* **32**, 20489–20498 (2021). <https://doi.org/10.1007/s10854-021-06558-2>
5. Moustafa M.S. Sanad, Shadia W. Arafat, Zein K. Heiba, Hassan Elshimy, Structural characterization and electrochemical performance of Ni-doped Co<sub>9</sub>S<sub>8</sub> for Li-ion battery and asymmetric supercapacitor dual applications, *Physica B: Condensed Matter*, 630 (2022):413707, <https://doi.org/10.1016/j.physb.2022.413707>.
6. M. Powalla, P. Stefan, H. Dimitrios, W. Roland, K. Friedrich, L. Peter, Advances in cost-efficient thin-film photovoltaics based on Cu(In, Ga)S<sub>2</sub>. *Engineering* **3**, 445–451 (2017). <https://doi.org/10.1016/j.eng.2017.04.015>
7. M. M. S. Sanad, A. M. Elseman, M. M. Elsenety, M. M. Rashad, B. A. Elsayed, Facile synthesis of sulfide-based chalcogenide as hole-transporting materials for cost-effective efficient perovskite solar cells, *J. Mater. Sci.: Mater. Electron.* **30** (2019): 6868–6875. <https://doi.org/10.1007/s10854-019-01001-z>.
8. I.M. Dharmadasa, A.P. Samantilleke, J. Young, M.H. Boyle, R. Bacewicz, A. Wolska, Electrodeposited p-type and n-type ZnSe layers for light-emitting devices and multi-layer tandem solar cells. *J. Mater. Sci: Mater. Electron.* **10**, 441–445 (1999). <https://doi.org/10.1023/a:1008922229057>
9. M. Altosaar, J. Raudoja, K. Timmo, M. Danilson, M. Grossberg, J. Krustok, Cu<sub>2</sub>Zn<sub>1-x</sub>Cd<sub>x</sub>Sn(Se<sub>1-y</sub>S<sub>y</sub>)<sub>4</sub> solid solutions as absorber materials for solar cells. *Phys. Status. Solidi. (A)* **205**, 167–170 (2008). <https://doi.org/10.1002/pssa.200776839>
10. M. M. S. Sanad, M. M. Rashad, A. Y. Shenouda, Novel CuIn<sub>1-x</sub>Ga<sub>x</sub>Te<sub>2</sub> structures for high-efficiency photoelectrochemical solar cells, *Int. J. Electrochem. Sci.* **205** (2016) 4337–4351, <https://doi.org/10.20964/2016.06.48>.
11. M. Kumar, C. Persson, Cu(Sb, Bi)(S, Se)<sub>2</sub> as indium-free absorber material with high optical efficiency. *Energy Procedia* **44**, 176–183 (2014). <https://doi.org/10.1016/j.egypro.2013.12.025>
12. M. Abdel-Latif, W. Magdy, T. Tosuke, A. Kanai, A. Hessein, N. Shaalan, A comprehensive study on Cu<sub>2</sub>SnS<sub>3</sub> prepared by sulfurization of Cu–Sn sputtered precursor for thin-film solar cell applications. *J. Mater. Sci.: Mater. Electron.* **31**(2020), 14577–14590. <https://doi.org/10.1007/s10854-020-04018-x>.
13. M. S. Eraky, M. M. S. Sanad, E. M. El-Sayed, A. Y. Shenouda, E. E. El-Sherefy, Phase transformation and photoelectrochemical characterization of Cu/Bi and Cu/Sb based selenide alloys as promising photoactive electrodes. *AIP Adv.* **9**(2019), 115115. <https://doi.org/10.1063/1.5120318>.
14. L. Jiyu, L. Jiang, B. Wang, F. Liu, J. Yang, D. Tang, Electrodeposition and characterization of copper bismuth selenide semiconductor thin films. *Electrochim. Acta.* **87**, 153–157 (2013). <https://doi.org/10.1016/j.electacta.2012.09.016>
15. A. Muthukannan, P. Prema, J. Henry, K. Mohanraj, G. Sivakumar, Photosensitivity of CuBiSe<sub>2</sub> thin film deposited by vacuum evaporation technique. *J. Chin. Chem. Soc.* **63**, 841–846 (2016). <https://doi.org/10.1002/jccs.201600189>
16. J. Elbenezar, Recent trends in material science, science and applications, Proceedings ICRTMSA, India, 2016
17. G. Zangari, Electrodeposition of alloys and compounds in the era of microelectronics and energy conversion technology. *Coatings* **5**, 195–218 (2015). <https://doi.org/10.3390/coatings5020195>
18. A. A. Pasa, M. L. Munford, Electrodeposition, E-ECHP. **8** (2006) 821–832. <https://doi.org/10.1081/E-ECHP-120037171>
19. M. Schlesinger, M. Paunovic, *Electrodeposition of semiconductors modern electroplating* (Wiley, New Jersey, United States, 2010)
20. P. Taxil, P. Chamelot, L. Massot, C. Hamel, Electrodeposition of alloys or compounds in molten salts and applications. *J. Min. Metall. B.* **39**, 177–200 (2003). <https://doi.org/10.2298/JMMB0302177T>
21. C. Agapescu, A. Cojocaru, A. Cotarta, T. Visan, Electrodeposition of bismuth, tellurium, and bismuth telluride thin films from choline chloride–oxalic acid ionic liquid. *J Appl. Electrochem.* **43**, 309–321 (2012). <https://doi.org/10.1007/s10800-012-0487-0>
22. M. Aguirre, N. H. Coavas, L. Fabetti, S. Urreta, Correction to nucleation and growth mechanisms in Cu–Co Films, *J. Phys. Chem. C.* **121** (2017) 25622–25622, <https://doi.org/10.1021/acs.jpcc.7b10414>
23. K. R. Mamaghani, S. M. Naghib, The Effect of stirring rate on electrodeposition of nanocrystalline nickel coatings and their corrosion behaviors and mechanical characteristics, *Int. J. Electrochem. Sci.* **12** (2017) 5023–5035. <https://doi.org/10.20964/2017.06.68>
24. A. Sharma, S. Bhattacharya, S. Das, K. Das, A study on the effect of pulse electrodeposition parameters on the morphology of pure tin coatings. *Metall. Mater. Trans. A* **45**, 4610–4622 (2014). <https://doi.org/10.1007/s11661-014-2389-8>
25. A. Bard, L. Faulkner, J. Brisset, *Electrochemical methods, fundamentals and applications* (Electrochimie, Paris, 1983)
26. A. Mallik, B.C. Ray, Evolution of principle and practice of electrodeposited thin film: a review on effect of temperature and sonication. *Int. J. Electrochem. Sci.* **4**, 1–16 (2011). <https://doi.org/10.4061/2011/568023>
27. H. Zhu, Y. Li, Y. Song, G. Zhao, W. Wu, S. Zhou, D. Wang, W. Xiao, Effects of cyclic voltammetric scan rates, scan time, temperatures and carbon addition on sulphation of Pb disc electrodes in aqueous H<sub>2</sub>SO<sub>4</sub>. *Mater. Technol.* **35**, 35–140 (2016). <https://doi.org/10.1080/10667857.2015.1133157>
28. H. Cesiulis, N. Tsyntsaru, A. Ramanavicius, G. Ragoisha, The study of thin films by electrochemical impedance spectroscopy. Springer, Berlin, Germany 2016. [https://doi.org/10.1007/978-3-319-30198-3\\_1](https://doi.org/10.1007/978-3-319-30198-3_1)
29. W. Huang, J. Li, Y. Xu, Nucleation/growth mechanisms and morphological evolution of porous MnO<sub>2</sub> coating deposited on graphite for supercapacitor. *Materials* **10** (2017) 1205. <https://doi.org/10.3390/ma10101205>
30. E. M. Elsayed, M. M. Moharam, I. A. Ibrahim, H. F. Y. Khalil, M. R. Hussein, M. M. B. El-Sabbah, Electrochemical-anodization synthesis of spinel cobalt ferrite films on various substrates from aqueous medium, *J. Basic Appl. Chem.* **8** (2018) 1–12,
31. L. Zhou, Y. Dai, H. Zhang, Y. Jia, J. Zhang, C. Li, Nucleation and growth of bismuth electrodeposition from alkaline electrolyte. *Bull. Korean. Chem. Soc.* **33**, 1541–1546 (2012). <https://doi.org/10.5012/bkcs.2012.33.5.1541>
32. D. S. Domínguez, A. Pardilla, B. Á. Murcia, E. Morallón, Z. D. Amorós, Electrochemical deposition of platinum nanoparticles on different carbon supports and conducting polymers, *J. Appl. Electrochem.* **38** (2007) 259–268. <https://doi.org/10.1007/s10800-007-9435-9>
33. S. Lai, R. Lazenby, P. Kirkman, P. Unwin, Nucleation, aggregative growth and detachment of metal nanoparticles during electrodeposition at electrode surfaces. *Chem. Sci.* **6**, 1126–1138 (2015). <https://doi.org/10.1039/C4SC02792B>
34. G. Karmakar, A. Tyagi, A. P. Wadawale, A. Y. Shah, G. Kedarnath, A. P. Srivastava, V. Singh, Accessing photoresponsive copper selenide nanomaterials and thin films through tetranuclear Cu(I) pyridylselenolate cluster. *J. Mater. Sci.* **55** (2020), 15439–15453. <https://doi.org/10.1007/s10853-020-05033-3>
35. S. Jeon, W. Choi, G. Song, Y. Son, D. Hur, Influence of surface roughness and agitation on the morphology of magnetite films electrodeposited on carbon steel substrates. *Coatings* **6**, 62–80 (2016). <https://doi.org/10.3390/coatings6040062>

36. M.A. Shah, Growth of uniform nanoparticles of platinum by an economical approach at relatively low temperature. *Scientia Iranica* **19**, 964–966 (2012). <https://doi.org/10.1016/j.scient.2012.02.027>
37. B. Łosiewicz, *Solid State Phenom.* **228**, 65–78 (2015). <https://doi.org/10.4028/www.scientific.net/SSP.228.65>
38. V.B. Ghanwat, S.S. Mali, C.S. Bagade, R.M. Mane, C.K. Hong, P.N. Bhosale, Thermoelectric properties of Indium (III)-doped copper antimony Selenide thin films deposited using a microwave-assisted technique. *Energy Technol.* **4**, 835–842 (2016). <https://doi.org/10.1002/ente.201500508>
39. G. Chen, W. Wang, J. Zhao, W. Yang, S. Chen, Z. Huang, R. Jian, H. Ruan, Study on the synthesis and formation mechanism of flower-like  $\text{Cu}_3\text{SbS}_4$  particles via microwave irradiation. *J. Alloys Compd.* **679**, 218–224 (2016). <https://doi.org/10.1016/j.jallcom.2016.04.042>
40. C. Ma, S. Din, W. Seo, J. Lee, Y. Kim, H. Jung, W. Yang,  $\text{BiVO}_4$  ternary photocatalyst co-modified with N-doped graphene nanodots and Ag nanoparticles for improved photocatalytic oxidation: a significant enhancement in photoinduced carrier separation and broad-spectrum light absorption. *Sep. Purif. Technol.* **264**, 118423–118432 (2021). <https://doi.org/10.1016/j.seppur.2021.118423>
41. <https://www.jp.xpssimplified.com/elements/bismuth.php>
42. J.F. Moulder, W.F. Stickle, P.E. Sobol, K.D. Bomben, *Handbook of X-ray photoelectron spectroscopy* (Perkin-Elmer Corporation, Physical Electronics Division, Eden Prairie, Minn, 1992)
43. S. İlkay, M. Biçer, Structural, morphological and optical properties of  $\text{Bi}_{2-x}\text{Sb}_x\text{Se}_3$  thin films grown by electrodeposition. *J. Alloys. Compd.* **509**, 1538–1543 (2011). <https://doi.org/10.1016/j.jallcom.2010.10.165>
44. N.A. Supriyanto, A.H. Ramelan, F. Nurosyid, Effect of annealing temperature on optical properties of  $\text{TiO}_2$  18 NR-T type thin film. *J. Phys.* **1011**, 012016 (2018). <https://doi.org/10.1088/1742-6596/1011/1/012016>
45. A. Hojabri, Structural and optical characterization of  $\text{ZrO}_2$  thin films grown on silicon and quartz substrates. *J Theor. Appl. Phys.* **10**, 219–224 (2016). <https://doi.org/10.1007/s40094-016-0218-8>
46. A. Muthukannan, J. Henry, K. Mohanraj, G. Sivakumar, S. Thanikaikarasan, The effect of postdeposition annealing on the structural and optoelectronic properties of copper bismuth Selenide thin films by PVD. *J. Mater. Sci. Mater. Electron.* **27**, 9947–9952 (2016). <https://doi.org/10.1007/s10854-016-5065-5>
47. R. Das, S. Pandey, Comparison of optical properties of bulk and nano crystalline thin films of CdS using different precursors. *Inter. J. Mater. Sci.* <https://doi.org/10.1038/s41598-017-15519-x>
48. M. Rabeha, N. Khedmia, M.A. Fodha, M. Kanzaria, The effect of thickness on optical band gap and N-type conductivity of  $\text{CuInS}_2$  thin films annealed in air atmosphere. *Energy Procedia* **44**, 52–60 (2014). <https://doi.org/10.1016/j.egypro.2013.12.009>
49. E.P. Mukhokosi, S.B. Krupanidhi, K.K. Nanda, Band gap engineering of hexagonal  $\text{SnSe}_2$  nanostructured thin films for infra-red photodetection. *Sci. Rep. Rts.* **7**, 15215 (2017). <https://doi.org/10.1038/s41598-017-15519-x>
50. M. Julian, U. Rau, J.H. Werner, Light absorption and emission in semiconductors with bandgap fluctuations, a study on  $\text{Cu(In, Ga)}_2\text{S}_2$  thin films. *J. Appl. Phys.* **101**, 113519 (2007). <https://doi.org/10.1063/1.2721768>
51. R. Yang, J. Cai, J. K. Lv, X. Wu, W. Wang, Z. Xu, M. Li, W. Xu, Fabrication of  $\text{TiO}_2$  hollow microspheres assembly from nanosheets ( $\text{TiO}_2$ -HMSs-NSs) with enhanced photoelectric conversion efficiency in DSSCs and photocatalytic activity, *Appl. Catal. B.* **210**(2017), 184–193. <https://doi.org/10.1016/j.apcatb.2017.03.064>.
52. M. Gloeckler, I. Sankin, Z. Zhao, CdTe solar cells at the threshold to 20% efficiency. *IEEE J. Photovolt.* **3**, 1389–1393 (2013). <https://doi.org/10.1109/jphotov.2013.2278661>
53. R.K. Pandey, Shikha Mishra, Sanjay Tiwari, P. Sahu, B.P. Chandra, Comparative study of performance of CdTe, CdSe and CdS thin films-based photoelectrochemical solar cells. *Solar Energy Mater Solar Cells* **60**(2000), 59–72